Available online at www.sciencedirect.com
ScienceDirect
Journal of the European Ceramic Society 26 (2006) 3705–3710
www.elsevier.com/locate/jeurceramsoc

Fabrication and microstructure of directionally solidified $SrCe_{1-x}Y_xO_{3-\delta}$ ($x = 0.1, 0.2$) high temperature proton conductors

J. Ramírez-Rico [a,*], M.J. López-Robledo [a], A.R. de Arellano-López [a], J. Martínez-Fernández [a], A. Sayir [b]

[a] *Departamento de Física de la Materia Condensada-ICMSE, Universidad de Sevilla-CSIC, Apdo, 1065, 41080 Sevilla, Spain*
[b] *NASA-Glenn Research Center, Lewis Field-21000 Brookpark Road-Mail Stop 106-1-Cleveland, OH 44135-3191, USA*

Received 17 June 2005; received in revised form 18 November 2005; accepted 3 December 2005
Available online 18 January 2006

Abstract

$SrCe_{1-x}Y_xO_{3-\delta}$ ($x = 0.1, 0.2$) high temperature proton conductors (HTPC) have been fabricated by directional solidification using a laser-heated float zone (LHFZ) method. The resulting microstructures have been studied using scanning electron microscopy (SEM), X-ray diffraction (XRD), transmission electron microscopy (TEM) and electron backscatter diffraction (EBSD). The LHFZ method produces a cellular microstructure consisting of crystalline cells embedded in an amorphous matrix, showing a strong biaxial texture. EBSD studies show that all the crystalline cells have their <0 0 1> axis as described in the cubic Pm3m prototype unit cell parallel to the growth direction. The observed microstructural features are explained in terms of the fabrication process.

Keywords: Laser processing; Perovskites; Fuel cells; Sr(Ce, Y)O_3; Proton conduction

1. Introduction

Since Iwahara and his collaborators discovered the proton conducting properties of rare earth-doped $SrCeO_3$,[1] great effort has been put in developing novel perovskites with enhanced ionic conductivity. Such perovskites, as $BaCeO_3$, $KTaO_3$ and $SrZrO_3$ have been found to be proton conducting when doped with trivalent ions occupying the B^{4+} sites in the perovskite ABO_3 structure.[2–7] This discovery has lead to a great interest in these materials for fuel cell, steam electrolyte, gas separation membranes, moist sensors and high-density energy storage applications.[8–11]

Despite the potential range of applications for these compounds, the conductivity of the as-fabricated materials has to be improved. Most of the studies found in the literature have been performed on sintered or hot-pressed samples,[1–6,8–12] for which the amount of impurities segregated on the grain boundaries played an important role in worsening the transport properties.

The laser-heated floating zone (LHFZ) method is a fast technique that produces nearly defect-free materials in a variety of processing conditions and shapes.[13–15] Depending on the solidification geometry, fibres and rods with diameters ranging from 200 μm to 4 mm can be produced. A flat geometry has also been developed, which can be used to deposit thick coatings on a variety of substrates.[16] This processing method produces very high thermal gradients within the sample, which are responsible for some of the novel microstructural features attainable.[17] In particular, it is possible to obtain highly textured materials with controlled microstructures by variation of the process parameters.

We have used the LHFZ method to fabricate directionally solidified $SrCe_{1-x}Y_xO_{3-\delta}$ ($x = 0.1, 0.2$). We expect this fabrication method to yield materials with novel microstructures and enhanced thermomechanical stability, both key factors in the development of improved high temperature proton conductors (HTPC).

The objective of this work is to demonstrate the possibility of fabricating HTPC by the LHFZ method and to illustrate the microstructural advantages this method has over the common sintering techniques.

* Corresponding author. Tel.: +34 954559758; fax: +34 954559753.
E-mail address: jrr@us.es (J. Ramírez-Rico).

0955-2219/$ – see front matter © 2005 Elsevier Ltd. All rights reserved.
doi:10.1016/j.jeurceramsoc.2005.12.003

2. Experimental procedures

2.1. Crystal growth

The $SrCe_{1-x}Y_xO_{3-\delta}$ samples were fabricated starting with high purity $SrCO_3$ (99.999% pure), CeO_2 (99.999% pure) and Y_2O_3 (99.99% pure) acquired to CERAC. The powders were mixed to the desired stoichometry and mechanically grinded for 40 h in an alumina mortar, and the resulting mixture was calcined for 6 h at 800 °C. The powder aggregates were milled, sieved and calcined again. The resulting powder was isostatically compacted at room temperature, yielding cylinder shaped pieces that were sintered for 10 h at 1500 °C in alumina crucibles. The whole process produced homogeneous, high-density cylinders with a diameter ranging from 4 to 5 mm, which were used as precursors for the laser-heated floating zone (LHFZ) apparatus.

The LHFZ system used a CO_2 laser splitted in two beams 180° apart from each other. Each beam was focused using ZnSe lenses into the topmost end of the polycrystalline precursor until a molten drop was formed. Then a high density (99,9%), high grain size (100 μm) polycrystalline Al_2O_3 seed was slowly brought near the precursor until it was wetted by the molten drop previously formed. The molten zone was thus maintained by surface tension between both solids (floating zone). The precursor was moved vertically through the beam incidence area, being continuously melted and solidified. Only a small fraction of the laser maximum power (2200 W) was used due to high absorption of the oxides to 10.6 μm radiation. The molten zone temperature was measured using an Infrared Thermal Monitor and estimated to oscillate between 1900 and 2000 °C in the hottest zone (centre of the melt), although the absolute temperature could not be measured because the melt emissivity was not known. The growth rate at which the precursor was moved through the laser beams was 500 mm/h without rotation.

After the LHFZ process, cylinders with a typical length of 100 mm and a diameter ranging from 3 to 4 mm were obtained. The diameter was quite irregular due to the high evaporation rate of the oxides that was observed during the melt growth.

2.2. Microstructural characterization and X-ray diffraction

Powder X-ray diffraction (XRD) was carried out on the as fabricated samples to check the crystalline structure and to measure the different lattice parameters as a function of the dopant concentration. Samples were manually grinded in an agate mortar. Powder diffractograms were obtained in a Bruker D8 diffractometer and the lattice parameters were determined by LeBail fitting using the LHPM-Rietica implementation of the LeBail and Rietveld algorithms.[18,19]

For observation in the scanning electron microscope (SEM) and electron backscatter diffraction (EBSD), transverse and longitudinal sections of the different samples were cut using a diamond saw and mechanically grinded and polished using diamond paste up to a grain size of 1/4 μm. A final polishing step was carried using a colloidal silica suspension for EBSD measurements. Due to the good electronic conductivity of $SrCeO_3$, no conductive coating was needed. SEM and EDS observations were carried out in a JEOL JSM-6460LV Standard SEM. EBSD analysis was performed using a TSL Digiview Camera mounted in a Philips XL-30 Conventional SEM. The OIM 3.0 software suite (TSL) was used both for acquisition and analysis of the EBSD data.

Transmission electron microscopy (TEM) specimens were prepared using a standard procedure. Transverse sections were cut and mechanically grinded, dimpled and then thinned using a Gatan PIPS ion polishing system. The observations were carried out in a Philips CM-200 TEM. Again, no conductive coating was required.

3. Results and discussion

3.1. X-ray diffraction

Our samples have the perovskite-related Pmna space group, as it has been previously reported for similar compositions in other work.[20] The obtained diffractograms are shown in Fig. 1, and the refined lattice parameters are contained in Table 1. The lattice parameters for $x = 0$ and $x = 0.15$ are from reference.[20] A small peak at about 26.6° can be observed in both samples, which corresponds to the <0 1 1> reflection of quartz ($d = 3.342(1)$ Å). This is attributed to contamination from the agate mortar during manual grinding. Fig. 2 shows the pseudocubic lattice volume as a function of the Y content. The lattice volume decreases with increasing dopant concentration as expected. However, the substitution of Y in the Ce sites of the perovskite structure leads

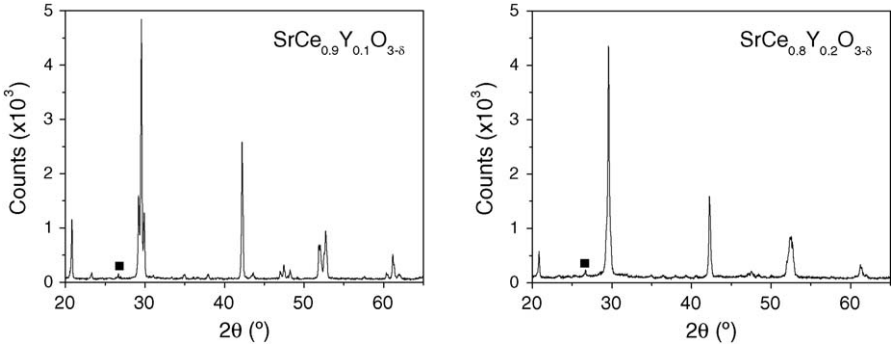

Fig. 1. X-ray powder diffractograms for $SrCe_{0.9}Y_{0.1}O_{3-\delta}$ and $SrCe_{0.8}Y_{0.2}O_{3-\delta}$. The peaks marked with a square (■) correspond to the <0 1 1> reflection of quartz ($d = 3.342(1)$ Å).

Table 1
Lattice parameters of $SrCe_{1-x}Y_xO_{3-\delta}$ for different Yttrium concentrations

[Y] (at.%)	a (Å)	b (Å)	c (Å)	Volume (Å^3)
0[a]	6.1530	8.5891	6.0118	79.4290
10	6.1472	8.5923	6.0061	79.3084
15[a]	6.1346	8.5787	5.9968	78.8983
20	6.1186	8.5759	6.0057	78.7835

[a] Values from reference.[20]

to a reduction of the lattice volume by means of cooperative BO_6 octahedra rotation and distortion, formation of O^{2-} vacancies and A-sites antiparallel shift. These factors are correlated to each other and therefore there is no simple relation between Y content and unit cell volume.[21]

The perovskite Pmna orthorhombic unit cell chosen was the one commonly used by other authors,[20] although sometimes is useful to describe an orthorhombic perovskite using the cubic prototype. For further discussion, we will refer to the lattice parameter of the cubic prototype as a_c. The approximate equivalence relations between lattice directions in the cubic and orthorhombic perovskite are:

$$[1\,0\,1]_c \sim [1\,0\,0]_o$$
$$[0\,1\,0]_c \sim [0\,1\,0]_o$$
$$[-1\,0\,1]_c \sim [0\,0\,1]_o$$

And, the approximate lattice parameter relations are:

$$a_o \sim c_o \sim \sqrt{2}a_c$$
$$b_o \sim 2a_c$$

3.2. Electron microscopy and EBSD

The microstructure of $SrCe_{0.9}Y_{0.1}O_{3-\delta}$ observed in a SEM is shown in Fig. 3, and consists of ellipsoid-shaped crystalline grains or cells (bright contrast) surrounded by another phase, which was revealed to be amorphous by means of TEM (Fig. 4). The microstructure of $SrCe_{0.8}Y_{0.2}O_{3-\delta}$ was found to be similar. Fig. 3e) shows the microstructure along the rod radius. Variations in the microstructure can be observed: both grains and amorphous phase decrease their size from the axis to the sample surface. This is common in samples fabricated by the LHFZ method as the solid-liquid growth front is no completely flat because of the radial temperature gradients. Some banding effects can be observed near the sample surface, which are associated with growth front fluctuations.

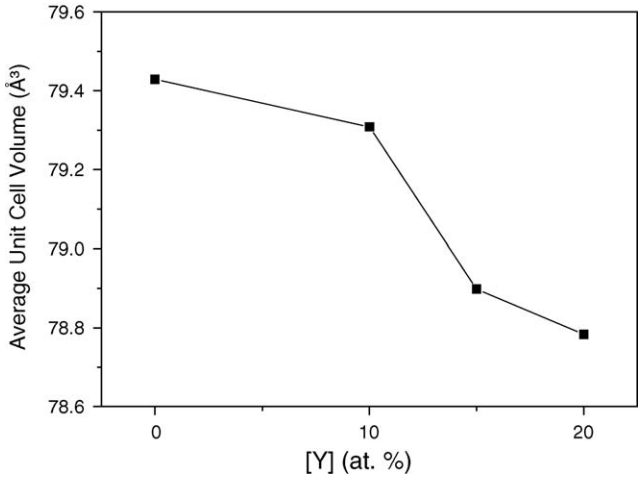

Fig. 2. Average unit cell volume as a function of Yttrium content. Data for $x = 0$ and $x = 0.15$ is taken from reference.[20]

EDS studies were carried out to determine the composition of both the crystalline cells and the surrounding amorphous phase. The cells were found to be very close to the expected stoichiometry in both samples, but the amorphous phase systematically exhibited a Ce deficit and about 3 mol% Al concentration in both compositions. Fig. 5 shows an EDS line scan across a glassy boundary in $SrCe_{0.9}Y_{0.1}O_{3-\delta}$, exhibiting the change in Ce concentration and the presence of Al. As in the LHFZ method the melt is floating and not in contact with a crucible or other material, the origin of Al can be traced to the milling of the precursor powders, for which an alumina mortar was used. On the other side, the origin of the amorphous phase can be attributed to the high evaporation rates of the precursor rods due to the high temperatures in the molten zone during the LHFZ process. The apparition of similar amorphous phases has been observed for other materials grown by a similar, laser-based technique. In a previous work,[22] the authors reported a similar microstructure for $LaAlO_3$ fibers grown by a laser heated floating method and attributed it to the evaporation of the precursor. In our scenario, the Al_2O_3 contaminant is present in the sintered precursor rods, and its molten along with the polycrystalline $SrCe_{1-x}Y_xO_{3-\delta}$. As the nucleation occurs, Al is diffused to the melt, accumulating at the grain boundaries and forming an Al-rich and Ce-poor liquid that solidifies as a glass. To estimate the average Al content in the bulk samples, several EDS spectrums were collected at different positions in the samples, from the center to the surface in a transversal sample. The Al content was always below 1 mol% everywhere in the sample, with an estimated average of 0.6 ± 0.1 mol%.

The cells show a number of plane defects as observed under the TEM, that correspond to domain interfaces. In the perovskite framework, a symmetry reduction occurs as the material is cooled, and the high temperature cubic phase transforms to orthorrombic, acquiring one of six possible orientations with respect to the original cubic orientation. The small differences in the lattice parameters of the pseudocubic unit cell make this mechanism plausible even if there is no phase transition and the material is orthorhombic up to the melting point. The planar defects inside the cells observed by means of TEM can be attributed to these phenomena, as it is evident after indexing of the SADP's from the different regions or domains. Fig. 4 shows two of those SADP corresponding to two adjacent domains. Using the choice of axes for the orthorhombic structure stated before it is clear that both domains had a common orientation in the cubic, high temperature phase. After the transition, however, different regions of the cell transform to different orientations, thus creating the planar defects observed.

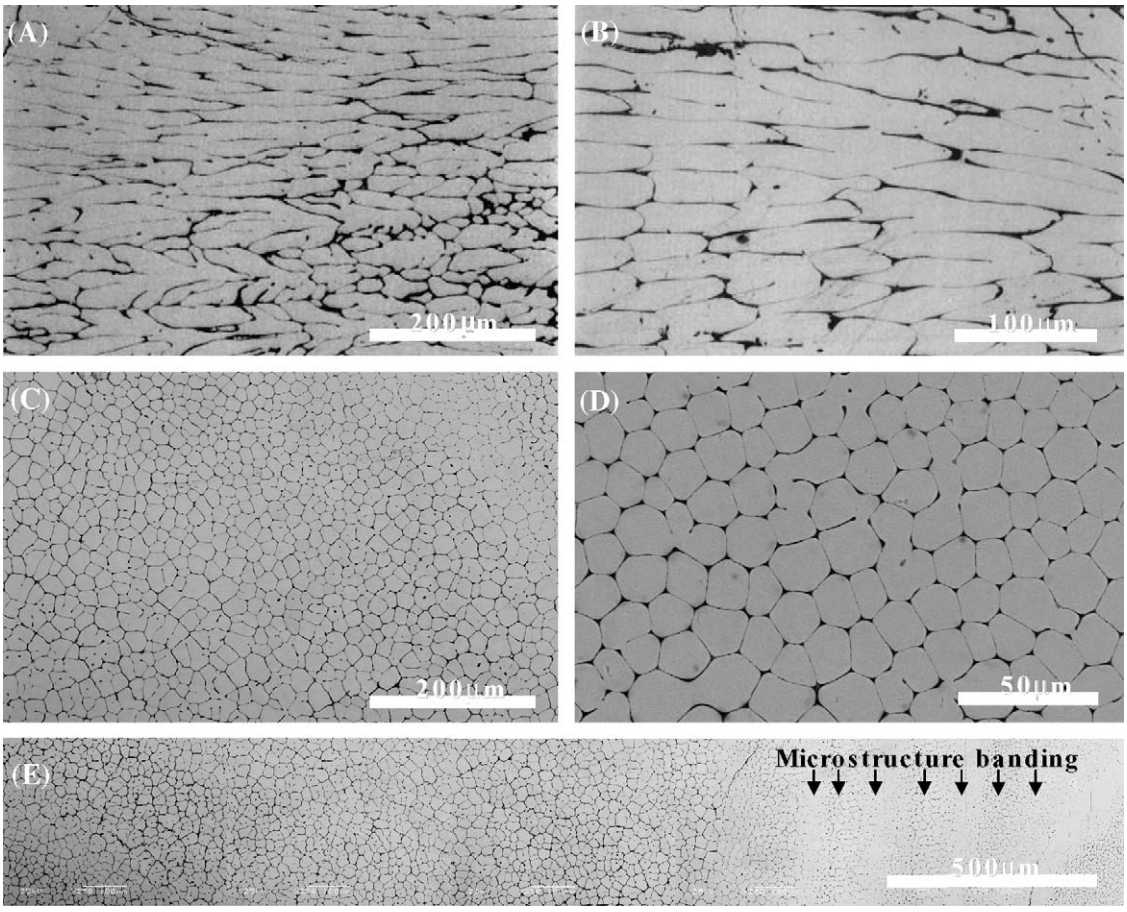

Fig. 3. SEM micrographs of $SrCe_{0.9}Y_{0.1}O_{3-\delta}$ samples in BSE contrast. (A) and (B) are longitudinal sections; while (C) and (D) are transversal sections. (E) represents the microstructure along the rod radius in a transversal section. Variations in the microstructure with the distance to the rod axis can be observed, as well as banding due to instabilities in the growth front.

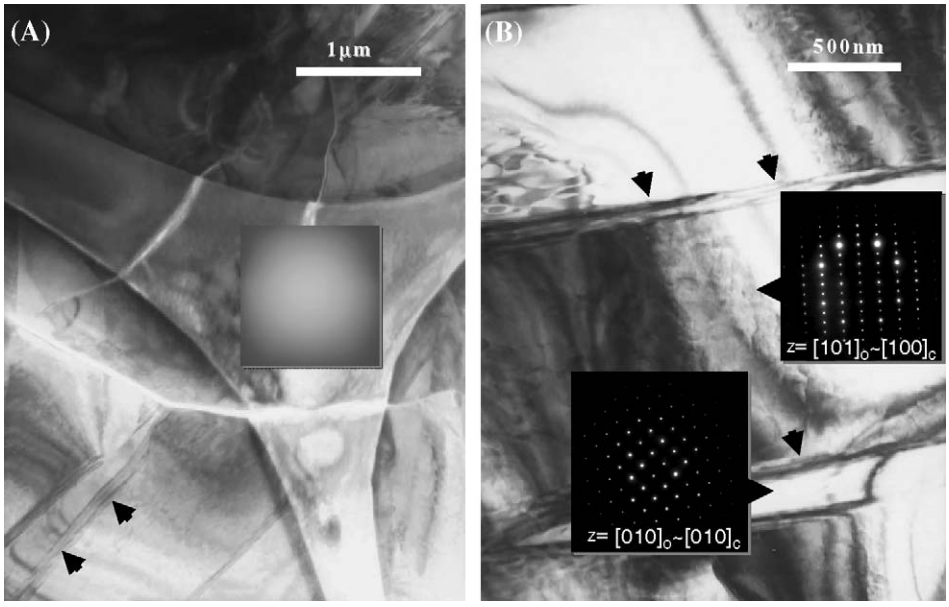

Fig. 4. TEM micrographs of $SrCe_{0.9}Y_{0.1}O_{3-\delta}$ samples. (A) Detail of a triple point and associated SADP obtained for the intergranular amorphous phase. (B) Detail of a cell showing crystallographic domain interfaces. Two SADP's are shown, corresponding to [0 1 0] and [1 0 1] zone axes in the orthorhombic structure which are approximately equivalent to <1 0 0> in the cubic prototype. Black arrows indicate domain interfaces.

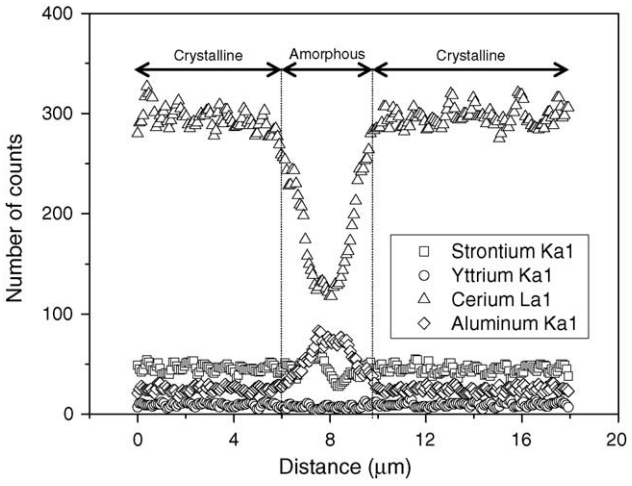

Fig. 5. EDS line scan taken across a cell boundary showing the relative change in Ce concentration and the presence of Al in the glassy intercellular phase.

Further evidence is brought by EBSD analysis of the sample. An area of $90 \times 120\,\mu m^2$ was scanned, acquiring and indexing more than 100,000 backscattering diffraction patterns. A cubic Pm3m structure was used for indexing, as the difference in lattice parameter in the orthorhombic structure is below the resolution of our EBSD apparatus and the orthorhombic and cubic structures could not be distinguished. Thus, our EBSD studies show the orientation data of the material before the cubic-to-orthorhombic phase transition that occurs as the material cools to room temperature after the LHFZ process. Fig. 6 shows the $\{0\,0\,1\}$ pole figure as was reconstructed from EBSD data. There is a clear biaxial texture that confirms that all the cells have the same crystallographic orientation. Our microstructure could therefore be described as that of a single crystal with precipitation of an amorphous phase, or a polycrystalline material with

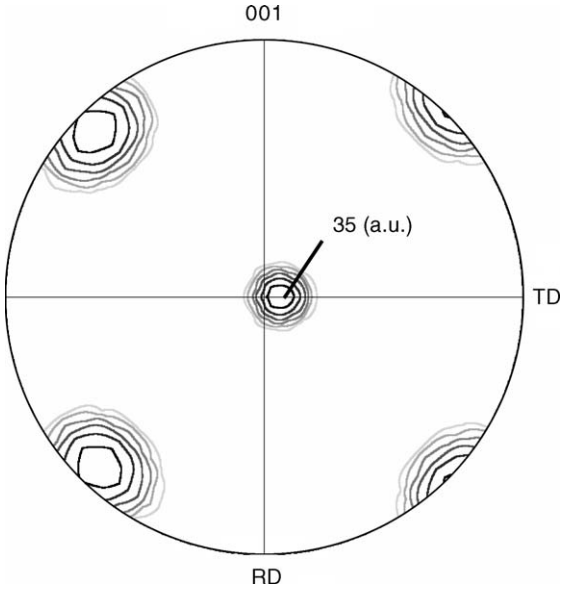

Fig. 6. $\{0\,0\,1\}$ Pole figure reconstructed from EBSD data assuming a cubic structure. A strong biaxial texture is clearly visible. The maximum intensity is 35 arbitrary units, the minimum is 1.

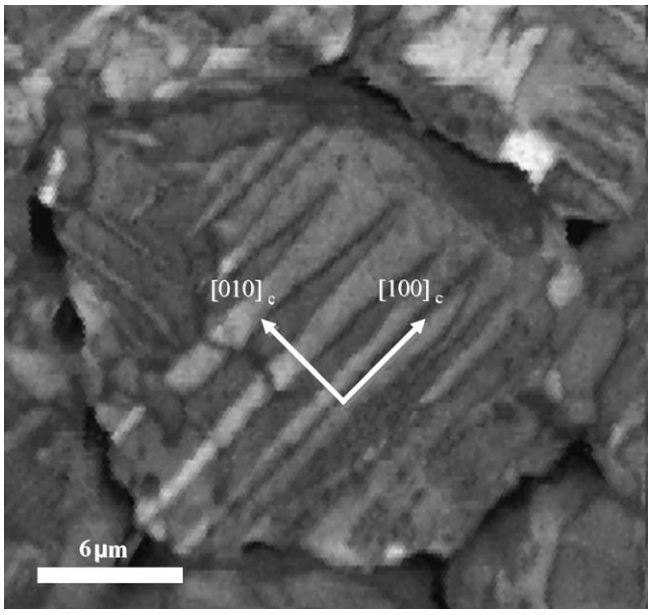

Fig. 7. Image quality (IQ) map obtained by EBSD from a single cell in transversal section. The main crystallographic axes in the cubic structure are shown to depict the nature of the domain interfaces.

strong crystallographic texture. Although not a single crystal, our material is expected to have better thermomechanical properties and stability than polycrystals, as has already been shown in a previous work.[23] It is not clear however what effect this amorphous phase will have on the transport properties, although it is expected to affect negatively compared to a pure single crystal. Further work geared towards reducing the amount of glassy phase is already in progress.

Fig. 7 shows an image quality map (IQ) of a transversal section of a cell of $SrCe_{0.9}Y_{0.1}O_{3-\delta}$ obtained by EBSD. The IQ factor is a measure of the contrast in the diffraction pattern and, among other variables, depends of the crystallographic orientation in the volume from where the pattern is acquired.[24] The IQ maps usually resemble those obtained by optical microscopy. Our previous observations in TEM are confirmed by EBSD, as the crystallographic domains are clearly visible in the IQ map shown in Fig. 7. The orientation of the main crystallographic axes in the cubic primitive is shown, confirming that the interface planes are $\{0\,0\,1\}$ planes in the cubic system.

4. Conclusions

Perovskite oxides for high temperature fuel cell applications have been successfully fabricated using a directional solidification technique. The resulting materials are highly homogeneous, with an orthorhombic Pmna structure, and their microstructure consists of large crystalline cells embedded in an amorphous matrix, which appears due to evaporation of the oxides at the high temperatures reached during de LHFZ process. Crystallographic domains are observed inside the crystalline cells, with six possible orientation variants and clear $\{0\,0\,1\}_c$ interfaces. A strong biaxial texture is observed in all the samples, with their $<0\,0\,1>_c$ direction aligned with the growth direction, which is

believed to be a consequence of the strong thermal gradients that appear during the directional solidification. Although controlling and reproducing the experimental growth conditions is difficult, a satisfactory relation between the fabrication parameters and microstructural features can be achieved.

Acknowledgements

This material is based upon work supported by the European Office of Aerospace Research and Development, Air Force Office of Scientific Research, Air Force Research Laboratory, under Grants No. FA8655-03-1-3040 and F61775-02-WE001. Any opinions, findings and conclusions or recommendations expressed in this material are those of the author(s) and do not necessarily reflect the views of the European Office of Aerospace Research and Development, Air Force Office of Scientific Research, Air Force Research Laboratory. The authors want to acknowledge the CITIUS Research Center at the Universidad de Sevilla for the use of their Electron Microscopy and X-ray diffraction Facilities. Joaquín Ramírez and Manuel Jesus López are grateful to the Junta de Andalucía for their predoctoral grants.

References

1. Iwahara, H., Esaka, T., Uchida, H. and Maeda, N., Proton conduction in sintered oxides and its application to steam electrolysis for hydrogen production. *Solid State Ionics*, 1981, **3/4**, 359–363.
2. Iwahara, H., Yajima, T. and Uchida, H., Effect of ionic radii of dopants on mixed ionic conduction ($H^+ + O^{2-}$) in $BaCeO_3$-based electrolytes. *Solid State Ionics*, 1994, **70/71**, 267–271.
3. Uchida, H., Maeda, N. and Iwahara, H., Relation between proton and hole conduction in $SrCeO_3$-based solid electrolytes. *Solid State Ionics*, 1983, **11**, 117–124.
4. Liang, K. C. and Nowick, A. S., High-temperature protonic conduction in mixed perovskite ceramics. *Solid State Ionics*, 1993, **61**, 77–81.
5. Nowick, A. S. and Du, Y., High-temperature protonic conductors with perovskite-related structures. *Solid State Ionics*, 1995, **77**, 137–146.
6. Reiche, U., Arons, R. R. and Schilling, W., Investigation of n-type electronic defect in protonic conductor. *Solid State Ionics*, 1996, **86–88**, 639–645.
7. Ma, G., Matsumoto, H. and Iwahara, H., Ionic conduction and nonstoichiometry in non-doped $Ba_xCeO_{3-\alpha}$. *Solid State Ionics*, 1999, **122**, 237–247.
8. Steele, B. C. H., Survey of materials selection for ceramics fuel cells. *Solid State Ionics*, 1996, **86–88**, 1223–1234.
9. Hagawa, T., Moe, K., Hiramatsu, T. and Goto, S., Design of electrodes for solid oxide fuel cells reactor. *Solid State Ionics*, 1998, **106**, 227–235.
10. Chen, C. H., Bouwmeeste, H. J. M., van Doorn, R. H. E., Kruidhof, H. and Burggraaf, A. J., Oxygen permeation of $La_{0.3}Sr_{0.7}CoO_{3-\delta}$. *Solid State Ionics*, 1997, **98**, 7–13.
11. Guan, J., Dorris, S. E., Balachandran, U. and Liu, M., Transport properties of $BaCe_{0.95}Y_{0.05}O_{3-\alpha}$ mixed conductors for hydrogen separation. *Solid State Ionics*, 1997, **100**, 45–52.
12. Flint, S. D., Hartmanova, M., Jones, J. S. and Slade, R. C. T., Microstructure of Ca-doped barium cerate electrodes. *Solid State Ionics*, 1996, **86–88**, 679–683.
13. Sayir, H., Farmer, S.C., Lagerlof, P. and Sayir, A., Advances in Ceramic-Matrix Composites II. In eds. Singh L.P. and Bansal N.P. American Ceramic Soc., 1994, pp. 53–63.
14. Sayir, A., Farmer, S. C., Dickerson, P. O. and Yun, H. M., High temperature mechanical properties of $Al_2O_3/ZrO_2(Y_2O_3)$ fibers. *Mater. Res. Soc. Symp. Proc.*, 1995, **365**, 21–27.
15. Sayir, A. and Farmer, S. C., The effect of microstructure on mechanical properties of directionally solidified $Al_2O_3/ZrO_2(Y_2O_3)$ eutectics. *Acta Mater.*, 2000, **48**, 4691–4697.
16. Merino, R. I., Peña, J. I., Laguna-Bercero, M. A., Larrea, A. and Orera, V. M., Directionally solidified calcia stabilised zirconia–nickel oxide plates in anode supported solid oxide fuel cells. *J. Eur. Ceram. Soc.*, 2004, **24**, 1349–1353.
17. Peña, J. I., Merino, R. I., Harlan, N. R., Larrea, A., de la Fuente, G. F. and Orera, V. M., Microstructure of Y_2O_3 doped Al_2O_3–ZrO_2 eutectics grown by the laser floating zone method. *J. Eur. Ceram. Soc.*, 2002, **22**, 2595–2602.
18. Le Bail, A., Duroy, H. and Fourquet, J. L., Ab-initio structure determination of $LiSbWO_6$ by X-ray powder diffraction. *Mater. Res. Bull.*, 1988, **23**, 447–452.
19. Hunter, B., Rietica—a visual rietveld program. International Union of the Crystallography Commission on Powder Diffraction Newsletter, 1998, 20. IUCr CPD, http://www.rietica.org.
20. Ranløv, J., Lebech, B. and Nielsen, K., Neutron diffraction investigation of the atomic defect structure of Y-doped $SrCeO_3$, a high-temperature protonic conductor. *J. Mater. Chem.*, 1995, **5**, 743–747.
21. Takeuchi, K., Loong, C. K., Richardson Jr., J. W., Guan, J., Dorris, S. E. and Balachandran, U., The crystal structures and phase transitions in Y-doped $BaCeO_3$: their dependence on Y concentration and hydrogen doping. *Solid State Ionics*, 2000, **138**, 63–77.
22. Andreeta, M.R.B., Andreeta, E.R.M. and Hernández, A.C., Laser-heated pedestal growth of colorless LaAlO3 single crystal fiber. *J. Cryst. Growth*, 2005, **275**, 757–761.
23. López-Robledo, M. J., Pinto-Gómez, A. R., Martínez-Fernández, J., de Arellano-López, A. R. and Sayir, A., Microestructura y propiedades mecánicas de Conductores Protónicos de Alta Temperatura crecidos por fusión de zona flotante. *Bol. Soc. Esp. Cerám. V.*, 2004, **43**, 753–758.
24. Schwarzer, R. A., Automated crystal lattice orientation mapping using a computer-controlled SEM. *Micron*, 1997, **28**, 249–265.